# Uncertainty Quantification of Seismic Imaging Using Neural Posterior Principal Components

**Julia Gao** [*]
Department of Computing and Mathematical Sciences
California Institute of Technology
Pasadena, CA 91125
juliagao10405@gmail.com


**Annika Viswesh** [*]
Department of Computing and Mathematical Sciences
California Institute of Technology
Pasadena, CA 91125
aviswesh@caltech.edu

## Abstract

Seismic hazard assessment and engineering planning rely on accurate velocity images of Earth's interior derived from travel-time data. Yet nonlinear wave physics, uneven station coverage, and the ill-posed inverse problem mean existing methods often return point estimates with little spatially resolved uncertainty. We propose a two-stage learning framework that combines a restoration network for predicting posterior-mean velocity images with a Neural Posterior Principal Components (NPPC) wrapper that learns low-dimensional modes of posterior variability. This adaptation of NPPC to seismic tomography produces uncertainty maps that explicitly link uncertainty structure to data coverage and acquisition geometry. On synthetic transmission and random-geometry datasets, our approach yields velocity images consistent with held-out data and uncertainty maps that expose stable versus underconstrained regions, offering the first spatially interpretable, data-driven uncertainty quantification framework for seismic travel-time tomography. Code base: UQ NPPC

## 1 Introduction

Accurate subsurface imaging through seismic tomography is fundamental to understanding the Earth's interior and assessing seismic hazards [1, 2]. Recent developments in high-resolution imaging leverage travel-time data from dense seismic networks, with regularization, Bayesian inference, or deep learning techniques to estimate subsurface velocity fields [3, 4, 5]. However, seismic data remains fundamentally limited by sparse sensor coverage, heterogeneity in noise, and uneven ray sampling, leading to significant spatial variability in model resolution [6, 7]. This necessitates uncertainty quantification for each region of the underlying velocity model [8, 9]. Many existing methods provide only point estimates or global uncertainty, leaving the spatial structure of uncertainty underexplored. In this work, we focus on quantifying and interpreting such uncertainties in seismic travel-time tomography. Achieving this requires a method that can both efficiently map observed data to an ensemble of plausible subsurface velocity fields and highlight the dominant modes of posterior variability. This, in turn, enables us to generate high-resolution uncertainty maps that track

---

[*]Denotes equal contribution

data coverage and subsurface structure, thereby providing insights into the regions where additional measurements would most reduce uncertainty.

**Travel-Time Tomography.** Seismic travel-time tomography aims to reconstruct a continuous velocity field from a discrete set of arrival-time measurements recorded by a network of seismic sensors [1, 10, 11]. The underlying physics relating the travel-time field to the velocity structure is described by the Eikonal equation, which is computationally challenging to solve for heterogeneous media [12, 13], as real-world seismic networks provide only sparse, noisy, and unevenly distributed measurements [6, 7]. Thus, traditional methods to manage the resulting ambiguity rely on strong regularization to produce a single, smooth solution [14, 15, 16]. However, these deterministic approaches do not characterize the underlying model uncertainty or its spatial structure [4, 5, 8].

**Deep Learning for Travel-Time Tomography**. Deep learning approaches to travel-time tomography can be organized by how they map travel-time observations to subsurface velocity models. Direct mapping architectures, such as U-Nets, learn to regress from observed travel times to dense pixel-wise velocity grids using supervised data. [3, 13, 17]. Neural solution operators learn mappings from entire travel-time fields to velocity models as continuous functions [18, 19, 20, 21]. Deep generative models address uncertainty quantification by learning to generate ensembles of velocity models consistent with travel-time data, providing posterior samples and global uncertainty maps [4, 5, 22, 23, 24, 25]. However, these models typically require heavy sampling and do not yield spatially interpretable uncertainty directly in the reconstructed velocity models [4, 25, 7].

**Uncertainty Quantification for Travel-Time Tomography**. Recent uncertainty quantification methods for travel-time tomography include variational inference [26, 27], conditional generative models [4, 23, 25], and ensemble-based approaches [5, 7]. While these techniques can generate posterior samples, they often require expensive sampling, suffer from training instability, or lack spatial interpretability. To overcome these challenges, we adapt Neural Posterior Principal Components (NPPC) [28] to seismic travel-time tomography. NPPC learns the dominant modes of posterior variability directly from residuals, producing spatially interpretable uncertainty maps that compactly summarize where models are stable and where they are underconstrained. Unlike sampling-based generative methods, NPPC captures these uncertainty structures in a single forward pass and enables systematic perturbations along learned directions. We demonstrate that NPPC provides the first uncertainty maps for travel-time tomography that explicitly reflect acquisition geometry, yielding compact and interpretable representations of uncertainty in velocity images.

## 2 Method

### 2.1 Dataset

We conduct experiments on a synthetic `FixedGrad` dataset, a collection of velocity fields generated with fixed gradient structure, paired with corresponding travel-time measurements. Each sample consists of a ground-truth velocity map $v_i \in \mathbb{R}^{28 \times 28}$ (km/s) and its first-arrival travel time observation $T_i$. Travel times are simulated using `PyKonal` with a fast-marching solver applied to the eikonal equation

$$\|\nabla T(\mathbf{x}; \mathbf{x}_s)\| = \frac{1}{v(\mathbf{x})}, \qquad T(\mathbf{x}_s) = 0, \tag{1}$$

where $T(\mathbf{x}; \mathbf{x}_s)$ denotes the travel time from source location $\mathbf{x}_s$, and $v(\mathbf{x})$ represents the local velocity field [13]. For each source, the travel-time field $T(\cdot; \mathbf{x}_s)$ is computed and then subsequently sampled at predefined receiver positions to obtain the observed travel times.

We evaluate two acquisition geometries, each containing 100,000 samples. In the `transmission` setting, $M$ sources are placed along one domain boundary and $N$ receivers along the opposite boundary ($M = N = 26$). For each source–receiver pair $(m, n)$, we record the first-arrival time $T_{mn}$. These discrete measurements are then arranged to form an $M \times N$ travel-time grid. In the `random` geometry, $M' = 10$ sources are sampled randomly along the boundary, while $N = 26$ receivers are fixed. The observed discrete travel times $\{T_{mn}\}$ are similarly arranged into an $M' \times N$ grid.
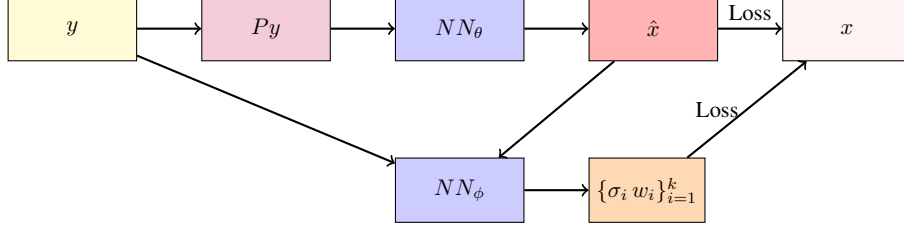
Figure 1: Formulation of our model. The travel-time observation $y$ is linearly projected to a $28 \times 28$ grid using $P$ and passed to the restoration network $NN_\theta$ to produce the posterior-mean velocity image $\hat{x}$. The prediction is trained against the ground-truth velocity image $x$. The NPPC head $NN_\phi$ takes $(y, \hat{x})$ and learns principal components $\{w_i\}$ and per-component scales $\{\sigma_i\}$ from the residual $e = x - \hat{x}$.

## 2.2 Model Architecture

Our model, illustrated in Figure 1, builds on the pretrained UNet from [28] training on the travel-time dataset, for velocity field restoration. A linear projection $P$ is applied to each travel-time observation $y \in \mathbb{R}^{M \times N}$, where $M \times N$ is either $10 \times 26$ or $26 \times 26$, mapping the input to a $28 \times 28$ latent space. The restoration network $f_\theta$ predicts the posterior-mean velocity image,

$$\hat{x} = f_\theta(Py), \tag{2}$$

where $\hat{x} \in \mathbb{R}^{28 \times 28}$.

To quantify uncertainty, we wrap the pretrained restoration model with a NPPC head. The NPPC network inherits the architecture of the restoration model, but increases the number of filters in the final layer by $k$, where $k$ is the number of principal components. This head learns $k$ principal component images $W = \{w_i\}_{i=1}^k$ (each $28 \times 28$), and per-component scales $\sigma = \{\sigma_i\}_{i=1}^k$, providing a low-rank basis for residual uncertainty.

We optimize a composite loss,

$$\mathcal{L} = \underbrace{\sum_i \|x_i - \hat{x}_i\|_1}_{L_\mu} + \lambda_1 \underbrace{\sum_i \|e_i - WW^\top e_i\|_2^2}_{L_\omega} + \lambda_2 \underbrace{\|W^\top W - I\|_F^2}_{L_\sigma} \tag{3}$$

where $e$ denotes the residual between the ground truth $x$ and the prediction $\hat{x}$. Here, $L_\mu$ enforces mean prediction accuracy, $L_\omega$ encourages the learned components to explain the residual, and $L_\sigma$ regularizes the components to be orthonormal.

In our implementation, the orthonormality constraint $\mathcal{L}_\sigma$ is enforced through explicit normalization of the principal component vectors during the forward pass rather than a penalty loss. For NPPC training phase, we set $\lambda_1 = 1$ for the reconstruction error and $\lambda_2 = \lambda(t)$, where $\lambda(t)$ follows a curriculum schedule that gradually increases from near-zero to 1 over the first 50 epochs of NPPC training, allowing the model to first learn principal directions before calibrating their magnitudes. Both $\mathcal{L}_\omega$ and the second-moment loss ($\lambda_2$) are normalized by the residual error norm $||e||_2$ on a per-sample basis, ensuring scale invariance and preventing either term from dominating the gradient signal.

At inference, uncertainty-perturbed velocity images are generated as

$$\hat{x} + \alpha \, \sigma_i \, w_i, \qquad \alpha \in [-2, 2], \tag{4}$$

for analysis of model uncertainty along principal directions.

The restoration network was trained for up to 140 epochs, while the NPPC head was trained for 100 epochs, with early stopping. Checkpoints were saved during training. Additional training details can be found in Appendix B.

## 2.3 Selection of Principal Components and Latent Space Dimensionality

**Principal Components (k)**. We set $k = 5$ following the original NPPC framework [28] , which demonstrated that dominant posterior uncertainty concentrates in a small number of modes. Each

principal component represent a distinct direction of variability in the posterior; too few components (e.g., k < 5) would underfit the posterior by missing important uncertainty modes, while too many components would produce redundant or negligible modes that traverse similar regions of the posterior without adding interpretable information.

**Latent Space Dimensionality**. The linear projection $P$ maps travel-time observations from their native acquisition geometry ($10 \times 26$ or $26 \times 26$) to a $28 \times 28$ latent representation matching the resolution of our ground-truth velocity fields. Since both acquisition geometries have fewer measurement than the target $28 \times 28$, this projection effectively upsamples the spares observations to the desired reconstruction resolution, allowig the restoration network to operate at a fixed spatial scale. The choice of $28 \times 28$ was determined by the synthetic dataset resolution; for higher-resolution applications, the latent space size should match the target velocity field reconstruction.

## 3 Results

| Geometry | RMSE | SNR | $2\sigma$ contain | $3\sigma$ contain | $z$-mean | $z$-std |
|---|---|---|---|---|---|---|
| Transmission | 0.201 | 28.18 | 0.948 | 0.991 | $-0.094$ | 1.012 |
| Random | 0.182 | 29.02 | 0.949 | 0.982 | 0.111 | 1.009 |

Table 1: Performance and uncertainty calibration metrics for NPPC on transmission and random geometries.



(a) Transmission geometry: Ground Truth
(b) Transmission geometry: Restoration
(c) Random geometry: Ground Truth
(d) Random geometry: Restoration



(e) Transmission geometry: Uncertainty
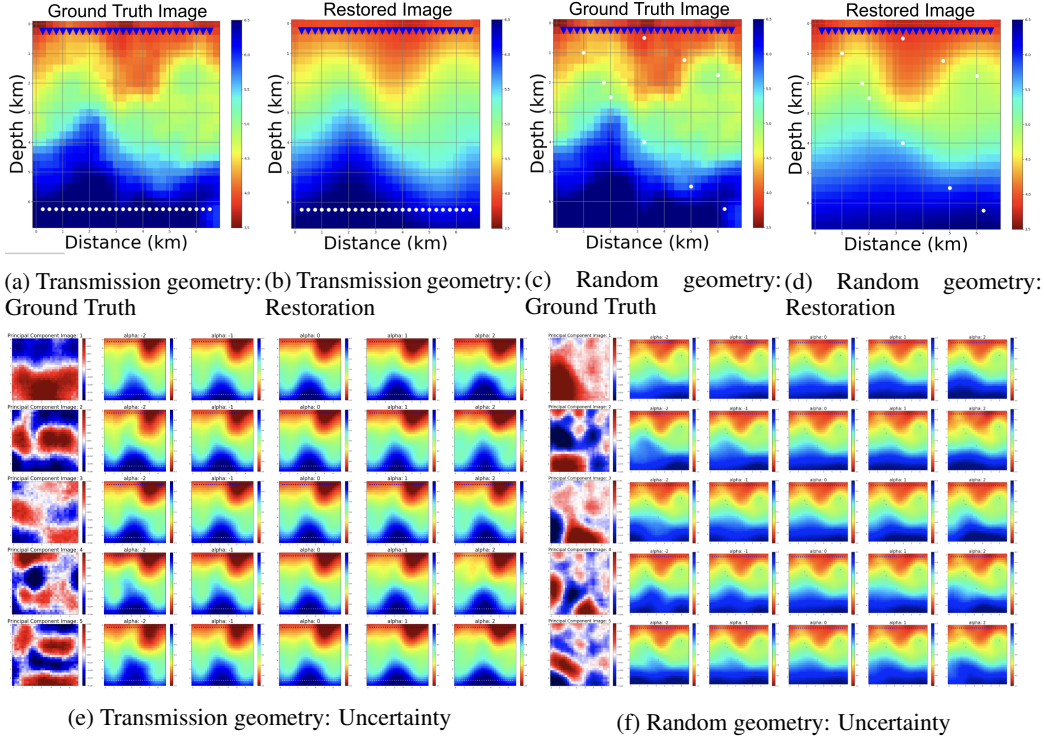
(f) Random geometry: Uncertainty

Figure 2: Uncertainty predictions from NPPC on two test geometries. (a) & (b) & (c) & (d) Restored velocity fields from the test set using the restoration model. (e) & (f) Corresponding NPPC uncertainty predictions, with each column showing a distinct test image and each row corresponding to one of the first five principal components. Each principal component traversal is visualized as $\hat{x} + \alpha\sigma_i\mathbf{w}_i$ with $\alpha \in \{-2, -1, 0, 1, 2\}$. White regions in the principal component maps indicate areas of high model confidence, while red and blue regions represent less confidence and greater uncertainty.

The quantitative metrics in Table 1 show that NPPC performs well across both acquisition settings. In the `transmission` geometry, the model reaches an RMSE of 0.201 km/s and an SNR of 28.18 dB. The $2\sigma$ and $3\sigma$ containment rates remain close to their nominal levels, and the $z$-mean and $z$-std values stay near zero and one, indicating calibrated predictive uncertainty. In the `random` geometry, NPPC achieves slightly lower RMSE (0.182 km/s) and higher SNR (29.02 dB). Coverage and calibration remain stable across both setups, with small differences consistent with the distribution of ray paths. Overall, the quantitative results show that NPPC maintains stable accuracy and calibrated uncertainty across both geometries.

Figure 2 shows reconstructed velocity fields and the corresponding NPPC uncertainty modes. For both geometries, the restored velocity fields closely match the ground-truth structure, recovering the main spatial features and gradients across the domain. Using the same sample for each geometry highlights that reconstruction quality remains stable despite differences in acquisition layout. Beyond the reconstructions themselves, the uncertainty modes provide insight into where the model is confident and where the data geometry leaves gaps. In the `transmission` geometry, the leading principal component consistently isolates variability along the vertical axis, which matches the alignment of the source and receiver arrays at the domain boundaries. Boundaries and peripheral regions show elevated uncertainty, particularly where ray paths are sparse or absent, while the central region remains stable. Traversals along higher principal components generate more diffuse or spatially disorganized uncertainty, with little coherence across images. While in the `random` geometry, the first component focuses variability in the lower left corner, a region with low ray density, while the upper right domain remains unchanged, consistent with dense receiver sampling. Higher-order components produce localized oscillatory changes in under-sampled regions, and in several cases, traversals visibly move the posterior estimate toward the ground-truth structure, indicating that the components act as correction modes aligned with gaps in data coverage. Furthermore, high-resolution features in the upper right of each component are stably reconstructed across all traversals, reflecting high ray density and model confidence. Across both acquisition setups, uncertainty modes are concentrated in regions that are not directly constrained by the measurement layout, confirming that principal component structure reflects the spatial distribution of ray coverage.

## 4   Discussion

We presented a framework for spatially resolved uncertainty quantification in seismic velocity imaging by adapting Neural Posterior Principal Components (NPPC) to travel-time tomography. The learned principal component images disentangle dominant modes of posterior variability, revealing how uncertainty concentrates in regions with sparse ray coverage or unfavorable source–receiver geometry, while stable features coincide with dense sampling. This provides the first interpretable link between acquisition geometry and spatial uncertainty in seismic velocity reconstructions. One of the limitations of our approach is that our data is restricted to synthetic waveform transmissions. Hence, we intend to evaluate the performance of NPPC on real-world synthetic data with complex noise sources, using datasets such as OpenFWI and European AlpArray. We also aim to benchmark NPPC against other sampling-based and Bayesian approaches such as UNET with Monte Carlo Dropout, to better evaluate the effectiveness of the method on travel-time tomography data. By connecting uncertainty structure to measurement coverage, our work offers a path toward data-informed survey design and more reliable seismic hazard assessment.
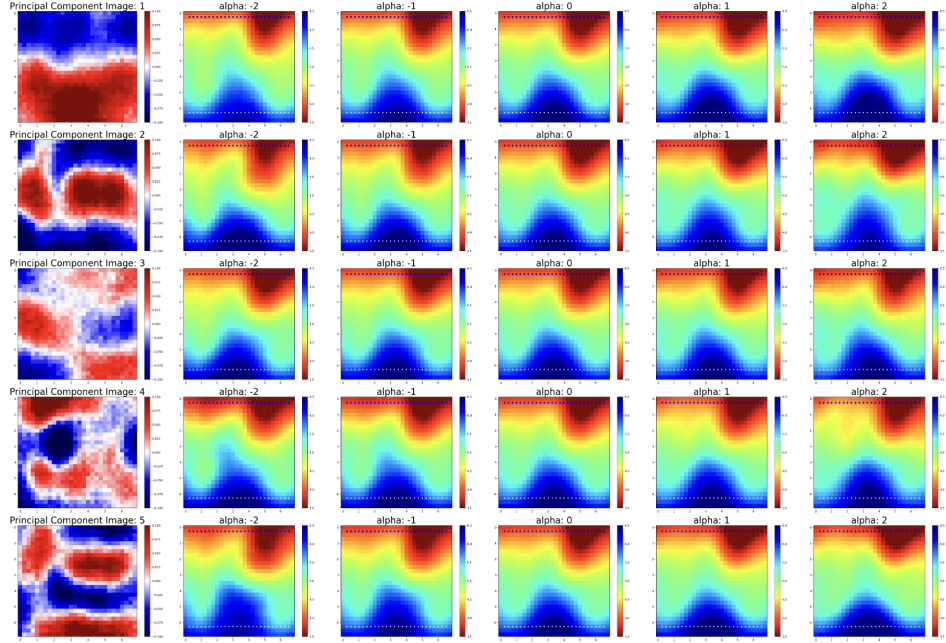
# References

[1] Guust Nolet. *A Breviary of Seismic Tomography: Imaging the Interior of the Earth and Sun*. Cambridge University Press, 2008.

[2] Clifford H. Thurber and Keiiti Aki. Three-dimensional seismic imaging. *Annual Review of Earth and Planetary Sciences*, 15:115–139, 1987.

[3] Katherine J. Bergen, Paula A. Johnson, Maarten V. de Hoop, and Gregory C. Beroza. Machine learning for data-driven discovery in solid earth geoscience. *Science*, 363(6433):eaau0323, 2019.

[4] Ali Siahkoohi, Gabrio Rizzuti, and Felix J. Herrmann. A deep-learning based bayesian approach to seismic imaging and uncertainty quantification. *arXiv preprint arXiv:2001.04567*, 2020.

[5] Ryoichiro Agata, Kazuya Shiraishi, and Gou Fujie. Physics-informed deep learning quantifies propagated uncertainty in seismic structure and hypocenter determination. *Scientific Reports*, 15:1846, 2025.

[6] Nick Rawlinson, Sara H. Pozgay, and Stewart Fishwick. Seismic tomography: A window into deep earth. *Physics of the Earth and Planetary Interiors*, 178(3-4):101–135, 2010.

[7] Luping Qu, Marcelo Araya-Polo, and Laurent Demanet. Uncertainty quantification in seismic inversion through integrated importance sampling and ensemble methods. *arXiv preprint arXiv:2409.06840*, 2024.

[8] Nicholas Rawlinson, Andreas Fichtner, Malcolm Sambridge, and Mallory K. Young. Seismic tomography and the assessment of uncertainty. *Advances in Geophysics*, 55:1–76, 2014.

[9] Yunduo Li, Yijie Zhang, Xueyu Zhu, and Jinghuai Gao. Seismic traveltime tomography based on ensemble kalman inversion. *Geophysical Journal International*, 240(1):290–302, 2025.

[10] Clifford H. Thurber. Earthquake locations and three-dimensional crustal structure in the coyote lake area, central california. *Journal of Geophysical Research: Solid Earth*, 88(B10):8226–8236, 1983.

[11] Jean Virieux, Arash Asnaashari, Rémi Brossier, Ludovic Métivier, Alice Ribodetti, and Wei Zhou. An introduction to full waveform inversion. In V. Grechka and K. Wapenaar, editors, *Encyclopedia of Exploration Geophysics*, pages R1–1–R1–40. Society of Exploration Geophysicists, 2014.

[12] James A. Sethian. A fast marching level set method for monotonically advancing fronts. *Proceedings of the National Academy of Sciences*, 93(4):1591–1595, 1996.

[13] Malcolm White, Hongjian Fang, Nori Nakata, and Yehuda Ben-Zion. PyKonal: A Python Package for Solving the Eikonal Equation in Spherical and Cartesian Coordinates Using the Fast Marching Method. *Seismological Research Letters*, 91(4):2378–2389, 2020.

[14] Lapo Boschi and Adam M. Dziewonski. High- and low-resolution images of the earth's mantle: Implications of different approaches to tomographic modeling. *Journal of Geophysical Research: Solid Earth*, 104(B11):25567–25594, 1999.

[15] Thomas Bodin, Malcolm Sambridge, Hrvoje Tkalčić, Pierre Arroucau, Kerry Gallagher, and Nick Rawlinson. Transdimensional inversion of receiver functions and surface wave dispersion. *Journal of Geophysical Research: Solid Earth*, 117(B2):B02301, 2012.

[16] William Menke. *Geophysical Data Analysis: Discrete Inverse Theory: MATLAB Edition*, volume 45 of *International Geophysics*. Academic Press, 3rd edition, 2012.

[17] Liyun Ma, Liguo Han, and Qiang Feng. Deep learning for high-resolution seismic imaging. *Scientific Reports*, 14:10319, 2024.

[18] Zongyi Li, Nikola B. Kovachki, Kamyar Azizzadenesheli, Burigede Liu, Kaushik Bhattacharya, Andrew M. Stuart, and Anima Anandkumar. Fourier neural operator for parametric partial differential equations. In *International Conference on Learning Representations*, 2021. ICLR 2021 (poster).

[19] Yan Yang, Angela F. Gao, Jorge C. Castellanos, Zachary E. Ross, Kamyar Azizzadenesheli, and Robert W. Clayton. Seismic wave propagation and inversion with neural operators. *The Seismic Record*, 1(3):126–134, 2021.

[20] Gege Wen, Zongyi Li, Kamyar Azizzadenesheli, Anima Anandkumar, and Sally M. Benson. U-fno—an enhanced fourier neural operator-based deep-learning model for multiphase flow. *Advances in Water Resources*, 163:104180, 2022.

[21] Nikola B. Kovachki, Zongyi Li, Burigede Liu, Kamyar Azizzadenesheli, Kaushik Bhattacharya, Andrew M. Stuart, and Anima Anandkumar. Neural operator: Learning maps between function spaces with applications to pdes. *Journal of Machine Learning Research*, 24(89):1–97, 2023.

[22] Shiran Levy, Jürg Hunziker, Eric Laloy, James Irving, and Niklas Linde. Using deep generative neural networks to account for model errors in markov chain monte carlo inversion. *Geophysical Journal International*, 228(2):1098–1118, 2022.

[23] Giovanni Angelo Meles, Macarena Amaya, Shiran Levy, Stefano Marelli, and Niklas Linde. Bayesian tomography using polynomial chaos expansion and deep generative networks. *Geophysical Journal International*, 237(1):31–48, 2024.

[24] Lukas Mosser, Olivier Dubrule, and Martin J. Blunt. Stochastic seismic waveform inversion using generative adversarial networks as a geological prior. *Mathematical Geosciences*, 52(1):53–79, 2020.

[25] Xuebin Zhao, Andrew Curtis, and Xin Zhang. Bayesian seismic tomography using normalizing flows. *Geophysical Journal International*, 228(1):213–239, 2022.

[26] Xin Zhang, Muhammad Atif Nawaz, Xuebin Zhao, and Andrew Curtis. An introduction to variational inference in geophysical inverse problems. In *Advances in Geophysics*, volume 62, pages 73–140. Elsevier, 2021.

[27] Xin Zhang and Andrew Curtis. Seismic tomography using variational inference methods. *Journal of Geophysical Research: Solid Earth*, 125(4):e2019JB018589, 2020.

[28] Elias Nehme, Omer Yair, and Tomer Michaeli. Uncertainty quantification via neural posterior principal components. *arXiv preprint arXiv:2309.15533*, 2023. NeurIPS 2023 Camera Ready, interactive examples available online.
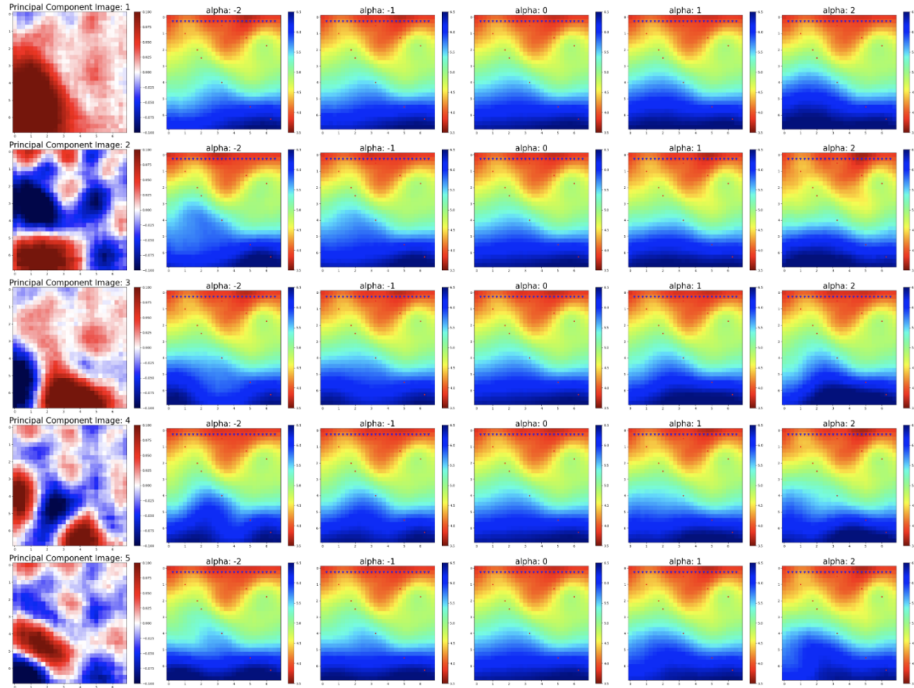
# A  Restoration Effect for Eikonal Data

# B  Additional Training Details

Both the restoration network and the NPPC head were trained with a learning rate of 1e-3 and optimized with Adam. The restoration network was trained for up to 140 epochs, while the NPPC head was trained for 100 epochs, with early stopping. Checkpoints were saved during training. All experiments were run on a single NVIDIA A40 GPU, and model selection was based on the lowest validation error.

(a) NPPC uncertainty predictions on the transmission geometry test set.



(b) Restoration results on the random geometry test set.

Figure 3: Enlarged visualizations of principal components for (a) NPPC uncertainty predictions on the transmission geometry test set and (b) restoration results on the random geometry test set.